Segmentation of Prostate Boundaries From Ultrasound Images Using Statistical Shape Model

Dinggang Shen*, Yiqiang Zhan, and Christos Davatzikos

Abstract—**This paper presents a statistical shape model for the automatic prostate segmentation in transrectal ultrasound images. A Gabor filter bank is first used to characterize the prostate boundaries in ultrasound images in both multiple scales and multiple orientations. The Gabor features are further reconstructed to be invariant to the rotation of the ultrasound probe and incorporated in the prostate model as image attributes for guiding the deformable segmentation. A hierarchical deformation strategy is then employed, in which the model adaptively focuses on the similarity of different Gabor features at different deformation stages using a multiresolution technique, i.e., coarse features first and fine features later. A number of successful experiments validate the algorithm.**

Index Terms—**Attribute vector, deformable registration, deformable segmentation, Gabor filter, hierarchical strategy, prostate segmentation, statistical shape model, ultrasound image.**

I. INTRODUCTION

PROSTATE cancer is the second-leading cause of cancer deaths in American men. The American Cancer Society predicted that in 2002, 189 000 men would be diagnosed with prostate cancer and about 30 200 would die [1]. When prostate cancer is diagnosed in its early stages, it is usually curable; and the treatment is often effective even in its later stages. Therefore, the decision of when, how, and on whom to apply a diagnostic procedure is very important [2].

Ultrasound (US) images of the prostate have been widely used for the diagnosis and treatment of prostate cancer [18]. US has been the main imaging modality for prostate related applications for various reasons: It is inexpensive and easy to use, it is not inferior to MRI or CT in terms of diagnostic value, and it can follow anatomical deformations in real-time during biopsy and

treatment. Therefore, various US images of the prostate have been used, for example, for needle biopsy [3], brachytherapy [4], and cancer treatment [5]. The accurate detection of prostate boundaries from the US images plays a key role in many applications, such as the accurate placement of the needles in biopsy [3], the assignment of the appropriate therapy in cancer treatment [4], and the measurement of the prostate gland volume [6].

Currently, in most applications the prostate boundaries are manually outlined from transrectal ultrasonography (TRUS) images, which is a tedious, time-consuming, and often irreproducible job. Therefore, a lot of work has been done to investigate automatic or semi-automatic algorithms that could segment the prostate boundaries from the ultrasound images accurately and effectively. Knoll *et al.* [7] developed a deformable segmentation model, by using a one-dimensional wavelet transform as a multiscale contour parameterization tool to constrain the shape of the prostate model. This method is implemented as a coarse to fine segmentation frame, based on a multiscale image edge representation. Ghanei *et al.* [8] designed a three-dimensional discrete deformable model to outline the prostate boundaries. The initialization of the model was manually produced by a set of human-drawn polygons in a number of slices, and it was simply deformed under both the internal force such as the curvature of the surface, and the external force such as edge map [9]. Pathak *et al.* [10] presented a new paradigm for the edge-guided delineation, by providing the algorithm-detected prostate edges as a visual guidance for the user to manually edit. The edge-detection algorithm is implemented in the following three stages. First, the stick-shaped filter is used to enhance the contrast and also reduce the speckle noise in the TRUS prostate images. Second, the resulting image is further smoothed using an anisotropic diffusion filter. Finally, some basic prior knowledge of the prostate such as shape and echo pattern is used to detect the most probable edges of the prostate.

In medical imaging, it is important to build deformable shape models that take into account the statistics of the underlying shape. So far, many statistical shape models have been developed to segment various structures from the human organs. Obviously, the use of statistical information greatly improves the performances of the developed models in the deformable segmentations. For example, Cootes *et al.* [11], [12], [20] have developed a technique for building compact models of the shape and appearance of variable structures in two-dimensional images, based on the statistics of labeled images that contain examples of the objects. Each model consists of a flexible shape template describing how the relative locations of important points

on the shapes can vary, and a statistical model of the expected gray-levels in a region around each model point. This method was further extended in [13]. Our group previously introduced an adaptive focus deformable model (AFDM) [14], which utilized the concept of an *attribute vector*, i.e., a vector of geometric attributes that was attached to each point on a surface model of an anatomical structure, and which reflected the geometric properties of the underlying structure from a local scale (e.g., curvature), to a global scale that reflected spatial relationships with more distant surface points. If the attribute vector is rich enough, it can differentiate between different parts of the shape that would otherwise look similar. An important aspect of using the attribute vectors is to provide a means for finding correspondences during the deformation.

However, the previous deformable models have limitations when applied to prostate segmentation. In this paper, we will present a statistical prostate shape model by using prior knowledge of the prostate in the US images, which is described next.

1) The ultrasound probe that was used to capture TRUS images appears as a dark disc in the TRUS images. Therefore, the location and the radius of the ultrasound probe can be easily detected.

2) The prostate is a walnut-shaped object, with the two parts of boundaries, i.e. the upper boundary and the lower boundary (c.f. Fig. 1). The lower boundary is always close to the boundary of the ultrasound probe, which results from the acquisition procedure of TRUS images. Therefore, the rough position of the prostate relative to the ultrasound probe can be simply represented by the orientation of a line connecting the centers of the ultrasound probe and the prostate. This can be used for the initialization of the prostate model.

3) The prostate boundary in the TRUS image can be identified as a dark-to-light transition of intensities from the inside of the prostate to the outside of the prostate. This property is particularly pronounced on the upper boundary in the majority of prostates (c.f. Fig. 1).

The proposed algorithm relies on two novel elements, i.e., *the Gabor filter bank representation of the prostate boundary in the ultrasound image* and *the hierarchical shape deformation strategy*. In most deformable models, the edge maps are usually used as image features to drive the deformation of the model. However, in the TRUS images of the prostate, the signal-to-noise ratio is very low, due to absorption and scattering. Therefore, it is difficult for the traditional edge detectors such as Canny edge detector to extract the correct boundaries of the prostate. In this paper, the Gabor filter bank [16] is used to characterize the prostate boundaries in a multiscale and multiorientation fashion. We select Gabor features for image representation for the following two reasons. First, each Gabor filter includes the Gaussian operation, which can remove the noise in the ultrasound images. Second, the Gabor filter bank includes the filters of multiorientations, which can provide the edge directions, and multiscales, which enable us to hierarchically focus on the similarity of different image features at different deformation stages. It is important to use the hierarchical deformation strategy in the prostate segmentation, since some
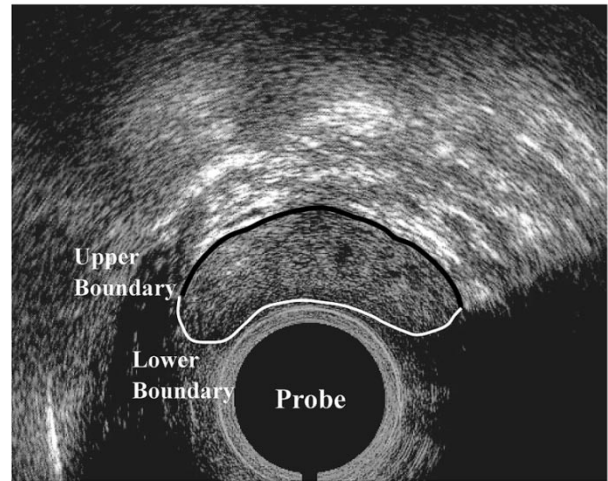

Fig. 1. Typical ultrasound image of the prostate. In this figure, the prostate is localized in the region that is encircled by the black and white contours, with the black providing the upper boundary of the prostate and the white providing the lower boundary of the prostate.

features such as the ultrasound probe are more reliable to be detected than others, while other features such as the prostate boundaries are usually very noisy and thereby cannot be identified directly. Since there exists a strong relationship between the position of the prostate and of the probe, we can first detect the location of the probe and then use the location of the ultrasound probe to roughly estimate the location of the prostate. In this paper, we employ two major hierarchical deformation strategies. First, since the Gabor bank evaluates image features at different levels, our model is designed to focus on the coarse features first and fine features later, so that the robustness of the algorithm is enhanced. Second, for each driving model point, the range of the searching domain and the length of the curve segment are hierarchically adjusted during the progression of the algorithm, so that they are large initially and decrease later. This increases the robustness of the algorithm and improves the accuracy of the final segmentation results.

II. METHODS

Our model consists of three major parts, i.e., the calculation of the statistical shape from the prostate samples, the hierarchical representation of the image features using the Gabor filter bank, and the hierarchical deformable segmentation. This is summarized in Fig. 2, and is briefly described in the following.

The shape statistics of the prostate can be calculated from a set of training samples that are manually outlined from their ultrasound images, which is similar to the approach used in [11]. However, the normalization of the prostate samples is different. In our approach, we normalize the prostate along with the ultrasound probe as follows. First, the shape of the ultrasound probe in the sample is normalized to that in the model. Simultaneously, the same transformation is performed on the prostate of the underlying sample. Second, the prostate in the sample is further normalized by rotating it around the center of the model's ultrasound probe, and also scaling it along the radial direction and

Model training

Multi-scale feature extraction

Training Samples

Detect probe center, position and radius

Manual outline

Manual boundary

Correspondence matching

Alignment

Aligned prostates

Principle component analysis

Statistical Model

Testing Sample

Detect probe center, position and radius

Smooth image

Smoothed image

Gabor filters

Gabor features

Construction of rotation-invariant Gabor features

Rotation Invariant Gabor Features

Hierarchical deformable segmentation

Initialization of the prostate model

Hierarchical deformation of the model

Corrected by statistical shape information

Deformed model
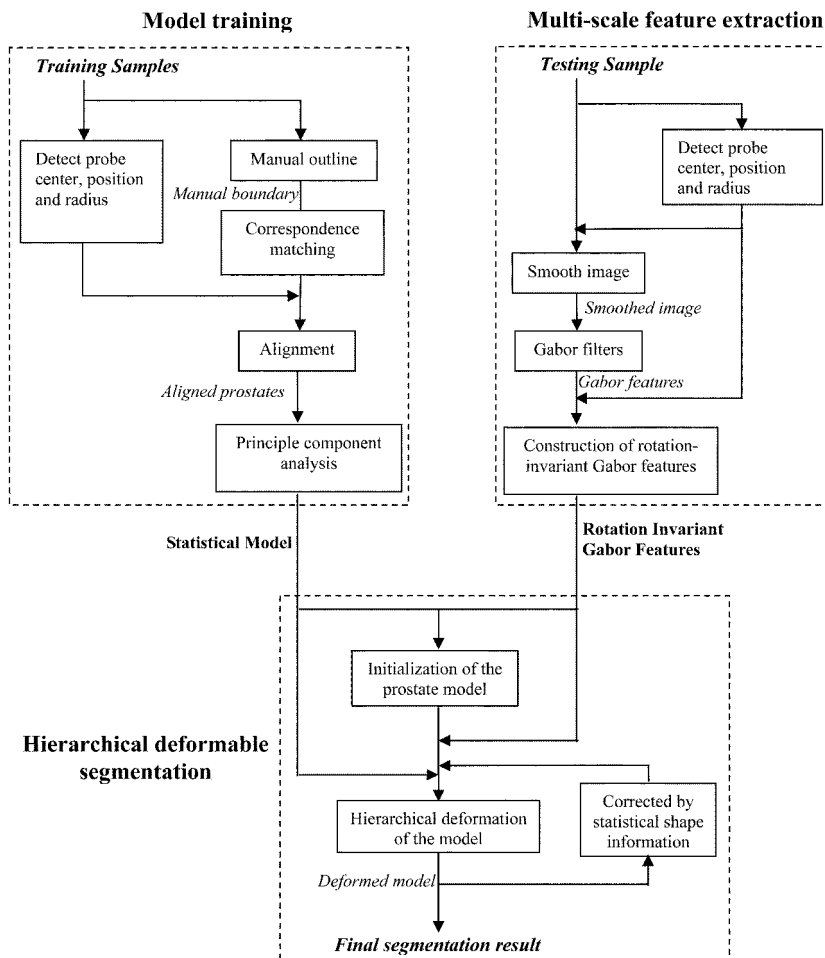
Final segmentation result

Fig. 2. Summary of the proposed algorithm for the prostate segmentation in the TRUS images.

the rotational direction of the model's ultrasound probe. The rotation degree and scaling sizes are determined directly from the correspondences between the model prostate and the sample prostate, which can be established by the affine-invariant feature-matching approach in [15].

The image features in the prostate image are hierarchically represented by a set of rotation-invariant features, which are reconstructed from the Gabor filter bank. Before calculating Gabor features, we first employ a small ellipse-shaped median filter, whose long axis passes through the center of the ultrasound probe, to remove noise in the ultrasound images. Notably, the regular Gabor features are not invariant to the rotation of the ultrasound probe. However, for each scale, we can resample and interpolate the Gabor features in the particular orientations, and make the reconstructed Gabor features invariant to the rotation of the probe. We use these rotation-invariant features as the image attributes for driving the prostate shape model to its correct position in the ultrasound image. Details of constructing the rotation-invariant Gabor features are described in Section II-A.

The initialization of the model is determined by rigidly transforming the average shape model to a pose that optimally matches with the rotation-invariant image features in the ultrasound image under study. Then, the model is hierarchically deformed under the forces from the image features and the

internal and statistical constraints respectively. The statistical constraint is fully used in the initial stage that makes the algorithm robust to local minima; it is designed to slacken gradually with the increase of the iterations, to make the final segmentation result accurate as well. The converged pose of the prostate shape model is regarded as the final segmentation result of the prostate from the underlying ultrasound image. Details of automatic initialization and hierarchical deformation strategy are given in Sections II-C and II-D, respectively.

A. Model Description

In this section, we will first provide the mathematical description of the prostate shape model and its transformation under a polar coordinate system. Then, we will give the multiscale and multiorientation representation of the image features from the TRUS images, using the Gabor filter bank. Both of these techniques will be used for the following sections.

1) Prostate Shape Model: The prostate shape model is represented by a set of ordered points, $C = \{V_i, i = 1, 2 \ldots, M\}$, which are equally sampled along the contour. In this paper, the average distance between two neighboring sample points is roughly two pixels (i.e. 0.8 mm), and there are $M = 100$ points in our prostate model. In the Cartesian coordinate system,

$V_i = (x_i, y_i)^T$. For describing the linear transformation of the prostate model, it is convenient for us to use the polar coordinate system with the origin at the probe center. In the polar coordinate system, the position of the prostate can be modeled as a rotation around the probe center and scalings along the radial direction and the rotational direction of the model's probe. Let us assume that, in the Cartesian coordinate system, the center of the probe is $(x_{\text{center}}, y_{\text{center}})^T$, and the radius of the probe is R_{probe}. Then, the prostate shape model under this new polar coordinate system becomes

$$C = \left\{ V_i = (r_i, \theta_i)^T, \qquad i = 1, 2, \ldots, M \right\} \tag{1}$$

where $r_i = \sqrt{(x_i - x_{\text{center}})^2 + (y_i - y_{\text{center}})^2} - R_{\text{probe}}$ and $\theta_i = \text{atan2}(x_i - x_{\text{center}}, y_i - y_{\text{center}})$. The definition of $\text{atan2}(x, y)$ is as follows:

$$\text{atan2}(x, y) = \begin{cases} \text{atan}\left(\frac{y}{x}\right), & x \geq 0, y \geq 0 \\ \text{atan}\left(\frac{y}{x}\right) + 2\pi, & x \geq 0, y < 0 \\ \text{atan}\left(\frac{y}{x}\right) + \pi, & x < 0. \end{cases} \tag{2}$$

The domain of θ_i is from 0 to 2π. Under this polar coordinate system, the transformations of the model (or other prostates) are constrained as rigid transformations, i.e., the scalings S_r and S_θ respectively on the dimensions r and θ, and the shifting T_θ on the dimension θ. Notably, the shifting on the dimension r is not suggested, since the lower boundary of the prostate is always close to the probe's boundary. Therefore, the total number of the parameters in the rigid transformation is three. Assume that the rigidly transformed model is $C' = \{V_i' = (r_i', \theta_i')^T, i = 1, 2, \ldots, M\}$. The relationship between C' and C can be mathematically described as follows:

$$\begin{aligned} C' &= T(C, S_r, S_\theta, T_\theta) \\ &= \left\{ V_i' = (r_i', \theta_i')^T, \begin{bmatrix} r_i' \\ \theta_i' \end{bmatrix} = \begin{bmatrix} S_r & 0 \\ 0 & S_\theta \end{bmatrix} \begin{bmatrix} r_i \\ \theta_i \end{bmatrix} + \begin{bmatrix} 0 \\ T_\theta \end{bmatrix} \right\}. \end{aligned} \tag{3}$$

By determining these three parameters, each prostate sample can be normalized to the space of the prostate model. Similarly, by adjusting these three parameters, the average shape model can be linearly transformed to the space of the prostate subject and used as initialization.

The transformation parameters (S_r, S_θ, and T_θ) between two prostate shapes can be directly determined by their correspondences, which can be established by our affine-invariant feature-matching approach in [15]. In this correspondence detection approach, we first define an affine-invariant attribute vector for each point V_i in the prostate shapes, in order to characterize the surrounding geometric structure. As demonstrated in Fig. 3, attributes used in this paper are the areas of the triangles formed by the point of interest (V_i) and its neighboring points (V_{i-vs} and V_{i+vs}), which is in some ways the extension of curvature. The area of the triangle, formed by the immediate neighbors, reflects local shape information around the point V_i. The areas of the larger triangles represent more global properties of the shape around the point V_i. It is not hard to see that the attribute vector corresponding to, say, a high-curvature region is completely different from the attribute vectors of flat segments. More important, the points of similar curvatures might have very different attribute vectors, depending on the number of components used in the attribute vector. For each point V_i, the areas that are calcu-
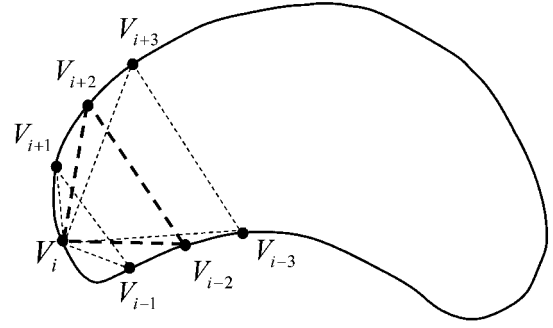

Fig. 3. Schematic explanation of the attribute vector. The area of a triangle formed by three points V_{i-vs}, V_i, and V_{i+vs}, is used as the $v$sth element of the attribute vector, defined for the point V_i.
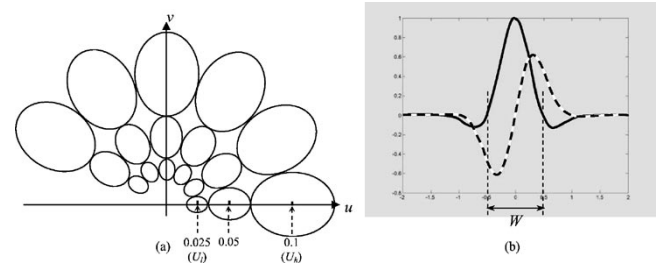

Fig. 4. Properties of Gabor filters using our selection of the parameters. (a) Frequency spectrum of the Gabor filters. The ellipse contour denotes the half-peak magnitude of the filter responses in the Gabor filter bank. The axes u and v respectively denote the horizontal and vertical spatial frequencies. U_l and U_h denote the lower and upper center frequencies of interest. (b) Mother Gabor function shown in one dimension, with the dashed line as the imaginary part and the solid line as the real part. W is the width for the main lobe of the real part of Gabor function.

lated from different neighborhood layers are stacked into an attribute vector $A(V_i)$, which can be further made affine-invariant by normalizing it across the whole shape, i.e.,

$$\hat{A}(V_i) = \frac{A(V_i)}{\frac{\sum_i \|A(V_i)\|}{\sum_i 1.0}} \tag{4}$$

where $\|A(V_i)\|$ is the magnitude of the vector $A(V_i)$. $\hat{A}(V_i)$ is the affine-invariant attribute vector for the ith point V_i. With the attribute vectors calculated, we can then determine the point correspondences across individual prostate shapes by examining the similarity of the underlying attribute vectors [15].

2) Multiscale Representation of Image Features: We use the Gabor filter bank to capture image features in multiscales and multiorientations [16]. For convenience, the Cartesian coordinate system is used here to describe the Gabor functions. The mother function of the two-dimensional Gabor filter is

$$g(x, y) = \left(\frac{1}{2\pi\sigma_x\sigma_y}\right) \exp\left[-\frac{1}{2}\left(\frac{x^2}{\sigma_x^2} + \frac{y^2}{\sigma_y^2}\right) + 2\pi jWx\right] \tag{5}$$

with the corresponding Fourier transformation as

$$G(u, v) = \exp\left\{-\frac{1}{2}\left[\frac{(u - W)^2}{\sigma_u^2} + \frac{v^2}{\sigma_v^2}\right]\right\} \tag{6}$$

where $\sigma_u = 1/2\pi\sigma_x$ and $\sigma_v = 1/2\pi\sigma_y$. W is a shifting parameter along the u axis in the frequency domain. The Gabor
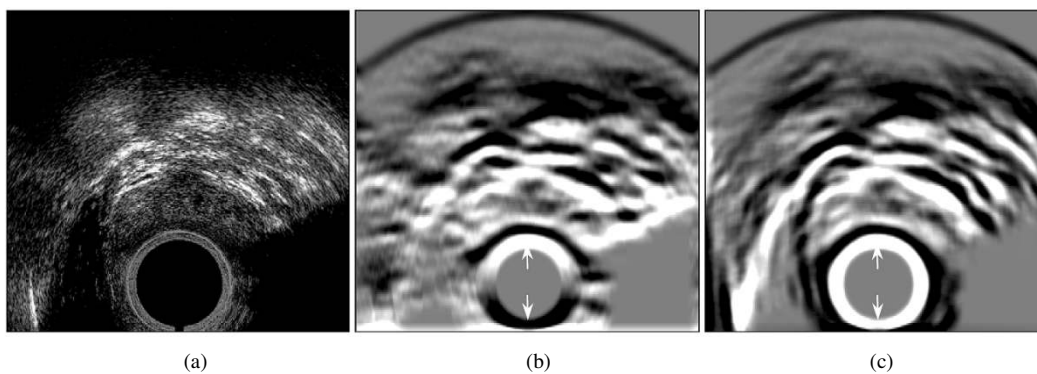
Fig. 5. Comparison of the regular Gabor features and the rotation-invariant Gabor features. (a) Original TRUS image. (b) Imaginary part of regular Gabor features $F_{0,0}(x,y)$, where the features in the probe boundaries indicated by the white arrows are different. (c) Imaginary part of the rotation-invariant Gabor features $\tilde{F}_{0,0}(x,y)$, where the features in the probe boundaries are isotropic. In both (b) and (c), the values of the Gabor features are normalized to 0–255, for display purposes.

filter bank can be obtained by the dilation and rotation of the mother function. Assume that the total numbers of the orientations and scales are, respectively, K and S, and the basic rotation and scale factors are, respectively, $\psi = \pi/K$ and $a = (U_h/U_l)^{1/S-1}$. Here, U_h and U_l are the parameters that determine the frequency range of the Gabor filter bank. As shown in Fig. 4(a), they are, respectively, the upper and lower center frequencies. a is the scaling step, used to scale the mother function. Using the scale variable $s\,(s = 0,\ldots,S-1)$ and the rotation variable $k\,(k = 0,\ldots,K-1)$, the (s,k)th Gabor filter is

$$g_{s,k}(x,y) = a^s g\left(a^s\left(x\cos(k\psi) + y\sin(k\psi)\right),\right.$$
$$\left. a^s\left(-x\sin(k\psi) + y\cos(k\psi)\right)\right). \qquad (7)$$

Therefore, for each pixel (x,y), we can obtain a vector of features $\{F_{s,k}(x,y), s = 0,\ldots,S-1; k = 0,\ldots,K-1\}$, where $F_{s,k}(x,y)$ is the (s,k)th Gabor feature calculated by the (s,k)th Gabor filter $g_{s,k}(x,y)$. Notably, the domain of the variable k is limited from 0 to $(K-1)$, since the Gabor features have the property, $F_{s,k+K}(x,y) = (F_{s,k}(x,y))^*$, where '*' is the conjugate operation. In order to let the half-peak magnitude support of the filter responses in the frequency spectrum touch each other as shown as ellipse contours in Fig. 4(a) [16], we use $\{K = 6, S = 3, U_h = 0.1, U_l = 0.025, W = U_h\}$, and also use the following formulas to compute the parameters σ_u and σ_v:

$$\sigma_u = \frac{(a-1)W}{(a+1)\sqrt{2\ln 2}} \qquad (8)$$

$$\sigma_v = \tan\left(\frac{\pi}{2K}\right)\left[W - 2\ln\left(\frac{\sigma_u^2}{W}\right)\right]\left[2\ln 2 - \frac{(2\ln 2)^2\sigma_u^2}{W^2}\right]^{-\frac{1}{2}} \qquad (9)$$

The Gabor filter bank has two important properties. First, as shown in Fig. 4(a), the frequency spectrum of the Gabor filter bank has a multiscale and multiorientation structure. Second, as a complex filter, each Gabor filter can be separated into two parts, i.e., the real part and the imaginary part. By appropriately selecting the parameters as given before, these two parts can be regarded respectively as a smooth filter and an edge detection filter. Fig. 4(b) shows the mother Gabor function in one dimension, where we can see that the imaginary part of the Gabor filter is exactly an edge detector and the real part is a smooth filter. Therefore, using the Gabor filter bank offers at least three advan-
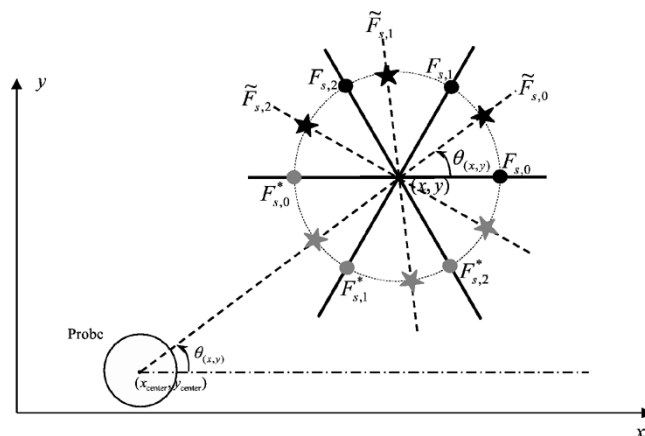

Fig. 6. Schematic explanation of the resampling principle for constructing the rotation-invariant Gabor features. The solid lines show the fixed orientations of the Gabor filters used to calculate regular Gabor features. The dashed lines show the actual orientations that we want to obtain the Gabor features. Notably, the Gabor features that are constructed at the orientations of the dashed lines are invariant to the rotation of the ultrasound probe. $\theta_{(x,y)}$ is the angle of an image pixel (x, y) in the polar coordinate system.

tages for prostate segmentation. First, with the Gaussian factor in the Gabor filter, the noise in TRUS image, such as speckle, can be smoothed or removed. Second, the multiscale structure of the Gabor filters enables the hierarchical implementation of our deformable model. Third, the multiorientation structure of the Gabor filters enables the extractions of edge direction as well as edge strength. Notably, as the prostate boundary in the TRUS image can be identified as a dark-to-light transition of intensities from the inside of the prostate to the outside, edge direction is an important feature to distinguish the prostate boundary from speckle noise. Compared to Pathak's stick-shaped filter [10], the Gabor filter bank provides rich edge maps that correspond to a variety of directions, rather than a single "maximum edge intensity" map.

However, the Gabor filter response is not invariant to the rotation of the probe, which can be considered equivalently as the rotation of prostate around the ultrasound probe. This is clearly shown in Fig. 5, with Fig. 5(a) as the original TRUS image and Fig. 5(b) as the imaginary part of the Gabor feature $F_{0,0}(x, y)$. Obviously, the Gabor features at the probe boundary are not consistent, as noted by the white arrows in Fig. 5(b). However, we
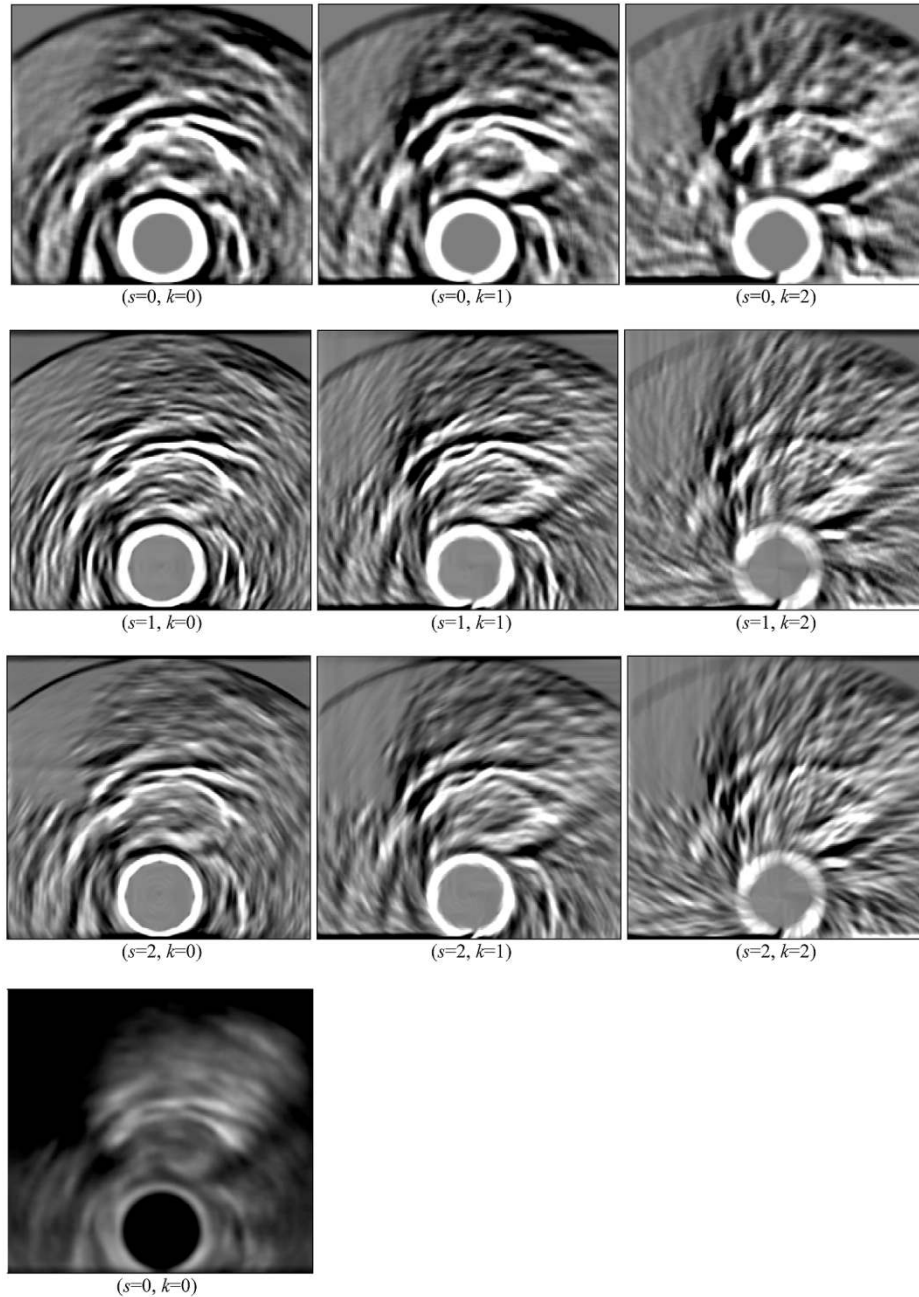
Fig. 7.   Rotation-invariant Gabor features at difference scales and different orientations. The first three rows show the imaginary part of rotation-invariant Gabor features; and the last row shows the real part of the one rotation-invariant Gabor feature. The values of the features are normalized to 0–255, for display purposes.

can obtain a set of rotation-invariant features by resampling and interpolating this set of regular Gabor features, with the first rotation-invariant feature as the output of the Gabor filter oriented at the angle $\theta_{(x,y)} = \text{atan2}(x - x_{\text{center}}, y - y_{\text{center}})$, where $(x_{\text{center}}, y_{\text{center}})^T$ is the coordinates of the probe center and (x, y) is a pixel under consideration. Let $\tilde{F}_{s,k}(x,y)$ denote the reconstructed Gabor features, which are calculated as follows:

$$\tilde{F}_{s,k}(x,y) = (1 - \beta)F_{s,k_0+k}(x,y)$$
$$+\beta F_{s,(k_0+1)+k}(x,y), \qquad k = 0, \dots, K - 1 \qquad (10)$$

where $k_0 = \lfloor \theta_{(x,y)}/\psi \rfloor$ and $\beta = (\theta_{(x,y)}/\psi) - k_0$. Notice that K is the total number of orientations and $\psi = \pi/K$. Using the property of the Gabor features $F_{s,k+K}(x,y) = (F_{s,k}(x,y))^*$,

the reconstruction of the rotation-invariant Gabor features will not increase the complexity order of the algorithm; that is, we only need to calculate the same K Gabor features for each scale s. The schematic explanation of this reconstruction principle is given in Fig. 6. For a pixel (x, y), the resulted rotation-invariant features in each scale s is $\{\tilde{F}_{s,0}(x,y), \dots, \tilde{F}_{s,K-1}(x,y)\}$, which can be separated into two parts, the imaginary part $\{\tilde{F}_{s,0}^{\text{Img}}(x,y), \dots, \tilde{F}_{s,K-1}^{\text{Img}}(x,y)\}$ and the real part $\{\tilde{F}_{s,0}^{\text{Real}}(x,y), \dots, \tilde{F}_{s,K-1}^{\text{Real}}(x,y)\}$. The imaginary part of the feature $\tilde{F}_{0,0}(x,y)$ is shown in Fig. 5(c), which is obviously isotropic, particularly in the probe boundary. Fig. 7 shows the imaginary part of the rotation-invariant Gabor features at three different scales and orientations, as well as

the real part of the Gabor feature at the scale $s = 0$ and the orientation $k = 0$.

B. Energy Function

The goal of our approach is to segment the prostates from the TRUS images, by minimizing the energy function of the prostate shape model. There are two energy terms, i.e., the external energy and the internal energy, in the whole energy function. The external energy is defined by the rotation-invariant Gabor features, and used to drive the deformation of the model to the prostate boundary. The internal energy is defined by the geometric attribute vectors, and used to preserve the geometric shape of the model during the deformation. The greedy algorithm is used as an optimization method to minimize the total energy function [14], [15], [17].

The total energy function that our model seeks to minimize is defined as

$$E = \sum_{i=1}^{M} E_i = \sum_{i=1}^{M} \left(w_{\text{Ext}} E_i^{\text{Ext}} + w_{\text{Int}} E_i^{\text{Int}} \right) \quad (11)$$

where E_i is the total energy on the ith model point (x_i, y_i), with the external and internal energy terms E_i^{Ext} and E_i^{Int}, respectively. The external energy term E_i^{Ext} drives the shape model to the prostate boundaries with the dark-to-light transitions of intensities, which is represented by Gabor features. The internal energy term E_i^{Int} preserves the geometric shape of the model during the deformation. w_{Ext} and w_{Int} are the two weighting parameters. The detailed definitions of these two energy terms are given next.

1) External Energy: According to our knowledge of TRUS, two criteria are used to design the external energy term. First, the prostate shape model should deform to the boundary positions with the dark-to-light transitions of intensities. This kind of boundary property can be captured by the imaginary part of the rotation-invariant features $\{\tilde{F}_{s,k}^{\text{Img}}(x, y)\}$, with $\tilde{F}_{s,k}^{\text{Img}}(x_i, y_i)$ being strong positive or strong negative according to our selected parameters for the Gabor filters (refer to Fig. 5 for an example). Second, for each model point, the image features in its neighborhood should match well with those in the TRUS image under study, where the matching degree can be defined by the real part of the rotation-invariant features $\{\tilde{F}_{s,k}^{\text{Real}}(x, y)\}$. Accordingly, the external energy function is defined as

$$E_i^{\text{Ext}} = w_{\text{Img}} E_i^{\text{Img}} + w_{\text{Real}} E_i^{\text{Real}} \quad (12)$$

where w_{Img} and w_{Real} are the two weighting parameters for two parts of the external energy term, E_i^{Img} and E_i^{Real}. In order to make the algorithm robust to the local minima, the parameter w_{Real} is designed to be large initially and decrease later, while the parameter w_{Img} is designed to increase during the progression of the algorithm.

E_i^{Img} is defined as

$$E_i^{\text{Img}} = \sum_{s=0}^{S-1} w_s \left(\sum_{k=0}^{K-1} -\tilde{F}_{s,k}^{\text{Img}}(x_i, y_i)(\vec{n}_k \bullet \vec{n}_i) \right) \quad (13)$$

where $\tilde{F}_{s,k}^{\text{Img}}(x_i, y_i)$ is the imaginary part of the rotation-invariant features at the deformed model position (x_i, y_i),
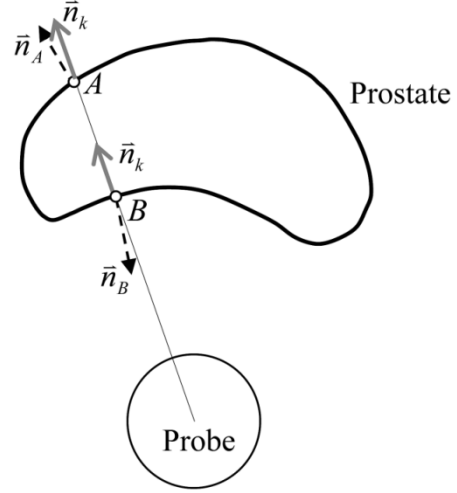

Fig. 8. Schematic explanation for the identical definition of the imaginary energy part E_i^{Img} on the upper and lower boundaries of the prostate. The black circle denotes the probe, and the walnut-shaped curve denotes the prostate. The points A and B denote the two model points on the upper and lower boundaries, respectively. The normal vectors on these two points are $\vec{n}_A$ and $\vec{n}_B$ respectively, and pointing in almost different directions. However, the directions of Gabor filters on these two points, $\vec{n}_k$, are the same. Since the polarities of the features, in the positions of the points A and B are also opposite, the imaginary energy part E_i^{Img} can, therefore, be defined identically on the upper and lower boundaries of the prostate.

with scale s and orientation k. $\vec{n}_k$ denotes the direction of the Gabor filter at the position (x_i, y_i), which is used to calculate the feature $\tilde{F}_{s,k}^{\text{Img}}(x_i, y_i)$. It is defined as $\vec{n}_k = [\cos(\theta_{(x_i, y_i)} + k\psi), \sin(\theta_{(x_i, y_i)} + k\psi)]^T$, where $\theta_{(x_i, y_i)} = \text{atan2}(x_i - x_{\text{center}}, y_i - y_{\text{center}})$ and $\psi = \pi/K$. $\vec{n}_i$ is the normal direction of the current model contour at the ith model point (x_i, y_i), which can be estimated directly by the positions of the already-ordered neighboring points. w_s is a weighting parameter.

Notably, the polarities of the Gabor features $\tilde{F}_{s,k}^{\text{Img}}(x_i, y_i)$ are opposite on the upper and lower boundaries of the prostate, due to the dark-to-light transition of intensities from the inside of the prostate to the outside of the prostate. The reason that these two parts can be represented identically in the external energy E_i^{Img} is given as follows. For example, the points A and B in Fig. 8 denote two model points respectively on the upper and lower boundaries of the prostate, and they have the same Gabor filter directions, $\vec{n}_k$. However, their normal vectors, $\vec{n}_A$ and $\vec{n}_B$, sit at almost opposite directions. Therefore, the dot products $(\vec{n}_k \bullet \vec{n}_A)$ and $(\vec{n}_k \bullet \vec{n}_B)$ have opposite signs. Considering the opposite signs of the Gabor features $\tilde{F}_{s,k}^{\text{Img}}(x_i, y_i)$ at the upper and lower boundaries and the opposite signs of the dot products between $(\vec{n}_k \bullet \vec{n}_A)$ and $(\vec{n}_k \bullet \vec{n}_B)$, the external energy E_i^{Img} on the upper and lower boundaries of the prostate have same signs and, therefore, can be represented identically.

E_i^{Real} is defined as the difference of the real parts of the rotation-invariant features respectively in the model's TRUS image and the underlying TRUS image. It is given as

$$E_i^{\text{Real}} = \sum_{\substack{\forall(x,y) \in N(x_i, y_i) \\ (x', y') \leftrightarrow (x, y)}} \sum_{k=0}^{K-1} \left(\tilde{F}_{0,k}^{\text{Real}}(x, y) - \overline{\tilde{F}_{0,k}^{\text{Real}}}(x', y') \right)^2 \quad (14)$$
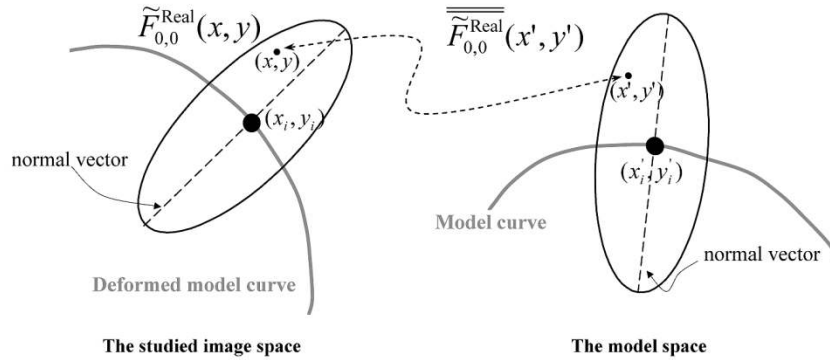
Fig. 9. Schematic explanation for the definition of the external energy part E_i^{Real}. The thick gray curve on the left is the deformed version of the model curve on the right. For the ith model point (x_i, y_i), the ellipse on the left corresponds to the ellipse on the right. Then the image features at (x, y) and its corresponding position (x', y') are compared. The total difference in the ellipse is defined as the external energy part E_i^{Real}.

where (x, y) is a point in the neighborhood of the ith model point (x_i, y_i) in the TRUS image under study. The point (x', y') is the corresponding point of (x, y) in the model space. $\overline{\tilde{F}_{0,k}^{\text{Real}}}(x', y')$ is the average feature calculated from the training samples at the position (x', y') in the model space. Please refer to Fig. 9, for schematic explanation of this strategy. Notably, according to the theory of signal processing, the dilation of a signal in the frequency field is equivalent to the shrinking in the spatial field. Therefore, the width of the main lobe for the real part of the Gabor filter becomes narrower and narrower with the increase of s [c.f. Fig. 4(b)], and the smoothing effect of the real part of the Gabor filter becomes less and less. Accordingly, we include only the coarse image features $\tilde{F}_{0,k}^{\text{Real}}(x, y)$, i.e., at the scale $s = 0$, for the definition of E_i^{Real}. This is different from the definition of E_i^{Img}.

Since the US prostate images are usually very noisy, there are a lot of spurious boundaries in the images, which are represented by the strong positive or strong negative imaginary part of the rotation-invariant Gabor features. If only using the external energy part E_i^{Img}, the prostate model possibly will be attracted by the spurious prostate boundaries. However, if we can check the similarity of the intensity distributions E_i^{Real} around the prostate boundaries of the model and the subject (as appearance model in [20]), we will have a better chance to avoid the spurious prostate boundaries. This surely makes the algorithm robust. The importance of using these two energy terms (E_i^{Img} and E_i^{Real}) jointly is clearly demonstrated by Fig. 13. In the upper-left corner of Fig. 13, the positions that are indicated by the solid and dashed arrows have the similar external energy part E_i^{Img}. However, when evaluating the external energy part E_i^{Real}, the position indicated by the dashed arrow has a much smaller image similarity than that indicated by the solid arrow. By jointly considering the two energy parts, the total external energy at the position indicated by solid arrow is much smaller than that indicated by dashed arrow. Therefore, the model is finally deformed to the position indicated by the solid arrow, providing the correct result.

2) Internal Energy: The internal energy is used to guarantee that each model point will be deformed to its corresponding position in the underlying TRUS image. We use an attribute vector to capture the geometry of the prostate shape in a hierarchical fashion. The attribute vector is attached to each point of the prostate model and reflects the geometric structure of the model
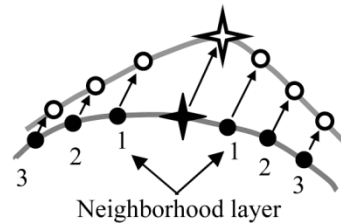

Fig. 10. Demonstration of the Gaussian displacement propagation. The star denotes the driving point under consideration, and the dots denote the points in the different neighborhood layer. Indexes 1–3 denote the neighborhood layers, relative to the driving point. The arrows denote the displacements calculated by a Gaussian propagation way.

from a global scale to a local scale [15]. Local scale attributes reflect differential geometric characteristics of the underlying structure, such as curvature, while global scale attributes capture spatial relationships among distant points. The attribute vectors are an important aspect of our model, since they provide a means of finding correspondences across individuals by examining the similarity of the underlying attribute vectors. We also use this similarity of attribute vectors to preserve the shape of the model during deformation. Accordingly, the internal energy function is defined as

$$E_i^{\text{Int}} = \left\| \hat{A}^{\text{Def}}(V_i) - \hat{A}^{\text{Mdl}}(V_i) \right\|^2 \tag{15}$$

where $\hat{A}^{\text{Def}}(V_i)$ and $\hat{A}^{\text{Mdl}}(V_i)$ are, respectively, the normalized attribute vectors of the deformed model and the average model at the point V_i. Notice that the attribute vectors are invariant to the affine transformation. Therefore, the internal energy function E_i^{Int} will not be affected by affine transformations. In the implementation, we can simply affine transform the curve segment of each model point to the pose where the transformed curve segment optimally matches with the image features in the underlying image.

C. Initialization

Initialization is crucial in deformable segmentation. For the algorithm to be effective in finding the expected objects, the deformable shape model must initially be placed close to the boundary of interest. The initialization process proposed in this paper is guided by the rotation-invariant Gabor features in the
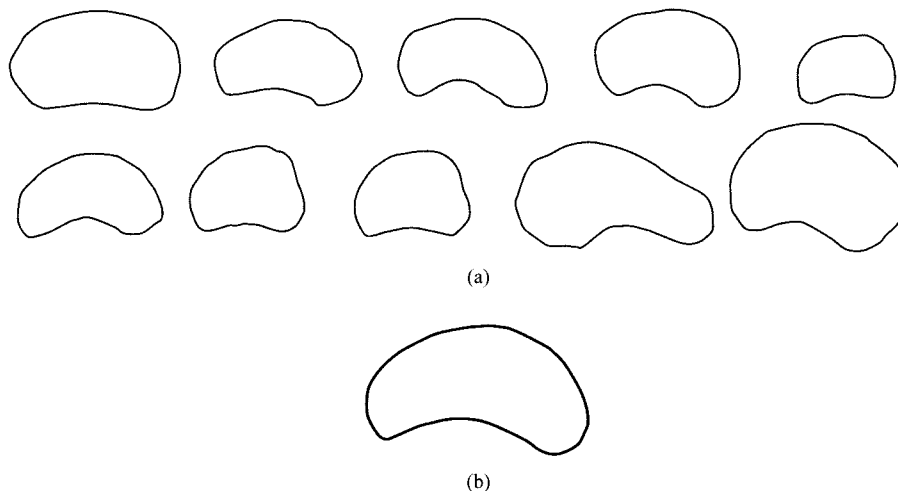
Fig. 11. Prostate model construction. (a) Ten manually delineated prostate boundaries. (b) Prostate model, which is created from the average shape of the ten aligned prostates in (a).

ultrasound images. In particular, we perform a series of rigid transformations [as described in (3)] on our prostate shape model, and for each transformation we calculate the difference degree of the corresponding rotation-invariant Gabor features in the model and in the underlying TRUS image. The initialization of the model is determined by a transformation that produces the minimal difference degree. The definition of the difference degree used in the initialization stage is similar to the definition of the external energy given in the previous Section II-B-1. In particular, we include the following three types of prior knowledge in defining the difference degree, for the purpose of initialization. First, the property of "dark-to-bright transition" in the upper boundary part of the prostate is much more consistent in the majority of prostate TRUS images, compared to that in the lower boundary (c.f. Fig. 1). So, we check the difference degree only on the upper boundary of the prostate. Second, we do not want the initialization result misled by noise, and we prefer fast implementation of the initialization. Therefore, we use the imaginary part of the *coarse* Gabor features to evaluate the difference degree of the rigidly transformed model with the object of interest in the underlying image. Third, the prostate in the underlying image is usually not a linearly transformed version of the prostate model; there usually exists nonlinear deformation between them. Because of this, even with an optimal linear transformation, not all of the model points can be exactly mapped to their corresponding feature points in the underlying image. Therefore, we should allow each transformed model point to search for the best match in its small neighborhood.

Mathematically, our initialization algorithm is formulated as follows:

$$\min_{S_r, S_\theta, T_\theta} D\left(C' = T(C, S_r, S_\theta, T_\theta)\right), \tag{16}$$

$$D\left(C' = T(C, S_r, S_\theta, T_\theta)\right) = \sum_{i \in \text{Upper boundary of } C'} D_i$$

$$= \sum_{i \in \text{Upper boundary of } C'} \min_{(x,y) \in N\left(x_i^{\text{Rigid}}, y_i^{\text{Rigid}}\right)}$$

$$\left(\sum_{k=0}^{K-1} -\tilde{F}_{0,k}^{\text{Img}}(x,y) \left(\vec{n}_k \bullet \vec{n}_{\left(x_i^{\text{Rigid}}, y_i^{\text{Rigid}}\right)}\right)\right)$$
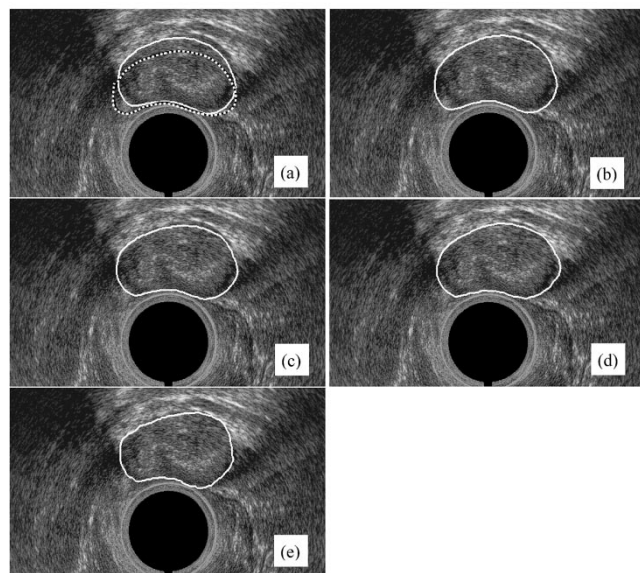

Fig. 12. Demonstration of the segmentation of the prostate in a TRUS image, using the proposed method. (a) Automatic initialization, where the dashed contour denotes the original model and the solid contour denotes the automatic initialization result. (b)–(d) The intermediate segmentation results, after 1, 4, and 12 iterations, respectively. (e) Final segmentation; the result of using total 20 iterations.

where C' is the rigid transformed version of the original model C, using three transformation parameters S_r, S_θ, T_θ, as described in (3). For each rigidly transformed model point $(x_i^{\text{Rigid}}, y_i^{\text{Rigid}})$ in the shape C', we look for the best match in its neighborhood $N(\cdot)$. The point (x, y) is one of the pixels in $N(\cdot)$, with the rotation-invariant Gabor feature $\tilde{F}_{0,k}^{\text{Img}}(x, y)$. $\vec{n}_k$ is the direction of the Gabor filter used to calculate the feature $\tilde{F}_{0,k}^{\text{Img}}(x, y)$. $\vec{n}_{\left(x_i^{\text{Rigid}}, y_i^{\text{Rigid}}\right)}$ is the normal vector of the model at the point $(x_i^{\text{Rigid}}, y_i^{\text{Rigid}})$. Fig. 12(a) gives an initialization example, with the original model shown as a dashed contour and its automatic initialization as a solid contour.

The initialization of the model is implemented as a global searching in the space of three transformation parameters. However, as the statistics of the prostate poses can be learned from
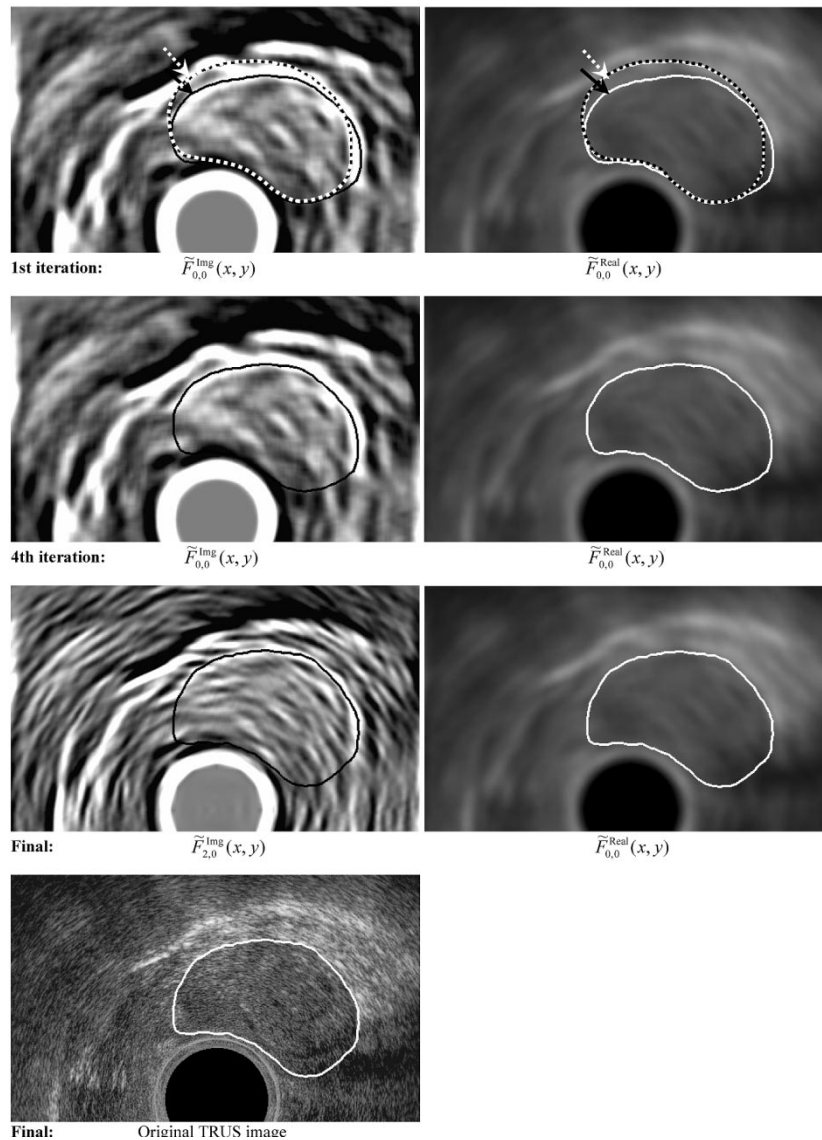
Fig. 13.   Demonstration of the importance of jointly using two external energy parts in the prostate segmentation. The first row shows the intermediate result, displayed, respectively, in the images of $\widetilde{F}_{0,0}^{\mathrm{Img}}(x,y)$ and $\widetilde{F}_{0,0}^{\mathrm{Real}}(x,y)$. The dashed contour denotes the automatic initialization of the model, and the solid contour denotes the deformed model after the first iteration. The second row shows the result after four iterations. The last two rows show the same final segmentation result in the image of $\widetilde{F}_{2,0}^{\mathrm{Img}}(x,y)$ the image of $\widetilde{F}_{0,0}^{\mathrm{Real}}(x,y)$, and the original TRUS image, respectively.

the training samples, the searching space can be limited in a small range. To further enhance the efficiency of the algorithm, we sparsely sample the parameter space. It should be mentioned here that the initialization result is not guaranteed to be perfect. However, our deformable segmentation algorithm is very robust, even in the case of bad initialization. This is shown in Fig. 14.

D. Hierarchical Deformation Strategy

The energy function that we want our algorithm to minimize contains a number of local minima. Although statistical shape information of the prostates used in this paper can help our algorithm reduce the chances of being trapped in local minima, we still need to design hierarchical deformation strategy for making our algorithm more robust and accurate [14], [15], [17]. The advantages of using the hierarchical deformation strategies were explained and demonstrated clearly in [14], [15], and [17]. In

this paper, two major hierarchical strategies are employed, i.e., the hierarchical focus of the rotation-invariant Gabor features in different deformation stages, and the hierarchical searching range and hierarchical curve segment length for each driving point.

1) Hierarchical Focus of the Gabor Features in Different Deformation Stages: According to the analysis in Section II-A, the Gabor filter bank outputs coarse features as well as fine features. This can be observed in Fig. 7. The coarse Gabor features are robust to the noise, while the fine Gabor features are sensitive to the noise. To make our algorithm robust to local minima, we must use these image features hierarchically. In particular, we minimize the energy terms that are defined by the coarse Gabor features in the initial deformation stages, including the initialization procedure. This makes the initialization and the initial model deformations robust to the noise. With the increase of the iterations, the model is deformed closer and closer to the
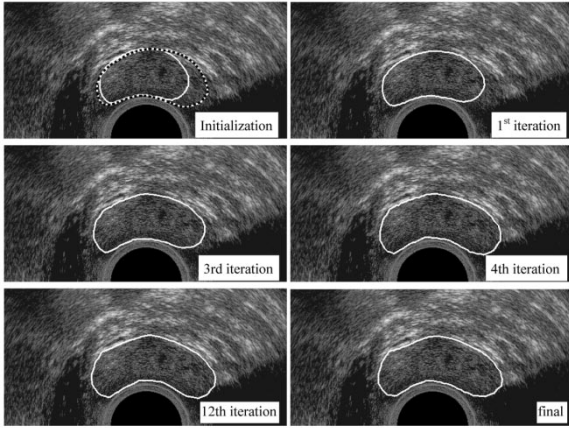
Fig. 14. Demonstration of the robustness of our algorithm with respect to the initialization. In the upper-left corner, the dashed contour denotes the original model, and the solid contour denotes the automatic initialization of the original model, which is far from the actual prostate boundary. The final segmentation results are shown in the right-bottom corner, with the intermediate segmentation results in the intervenient figures. This example shows the robustness of our algorithm in segmenting prostates, even in the case of the bad initialization.
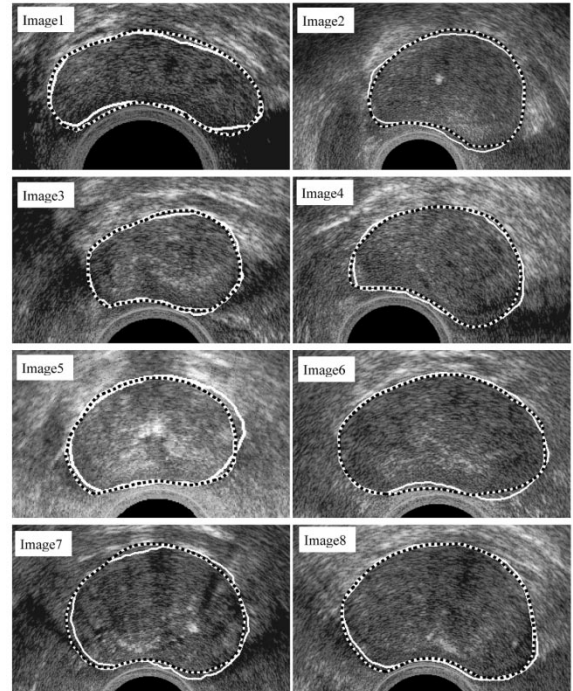

Fig. 15. Comparison of algorithm-based segmentations and manual segmentations, with the dashed contours as the manual segmentations and the solid contours as the algorithm-based segmentations. From the results, we can conclude that algorithm-based segmentation is visually as good as manual segmentation. The detailed differences between the algorithm-based and manual segmentations are summarized in Table I.

prostate boundary. To enhance the accuracy of the algorithm, the fine features are used to replace the coarse features, therefore, we transfer to minimize the energy functions that are defined by the fine features. The implementation of this hierarchical deformation strategy can be completed by dynamically adjusting the weighting parameter w_s of (13), during the deformation procedure.

2) Hierarchical Searching Range and Curve Segment Length for the Each Driving Point: For each driving point, its displacement is propagated to its neighboring model points at the Gaussian way. Mathematically, the propagation of the displacement can be described as

$$\vec{d_i} = e^{-\frac{i^2}{2L^2}} \vec{d_0} \qquad (17)$$

where $\vec{d_0}$ is the displacement on a driving point. The vector $\vec{d_i}$ is the displacement on the points in the ith neighborhood layer of the driving point under consideration. L is a parameter that controls the propagation range. Fig. 10 gives an example of this displacement propagation.

When evaluating whether the current displacement is optimal for this driving point, we calculate and compare the total energies on the curve segment, rather than only the energy on the driving point. The length of the curve segment around each driving point is large initially, and is designed to decrease later. Similarly, the size of the searching range, which is large initially, is designed to decrease as the iterations increase.

III. EXPERIMENTAL RESULTS

In this section, we describe four experiments on the segmentation of the prostate in TRUS images. The first example shows a complete procedure of our algorithm in segmenting a typical prostate. Our prostate model is an average shape of the ten aligned prostates, which are manually drawn from ten TRUS images. The model and ten training samples are shown in Fig. 11. Fig. 12 demonstrates a typical segmentation procedure on a TRUS image, with the original model as a dashed contour

in Fig.12(a). The original model was automatically initialized as a solid contour in Fig. 12(a). The initialized model is iteratively deformed under forces derived from the image features, the internal constraints, and the statistical shape information (calculated from ten manually drawn prostates as shown in Fig. 11). The intermediate segmentation results are displayed in Fig. 12(b)–(d), respectively. The final segmentation result is shown in Fig. 12(e).

In the second example, we show that jointly using the two external energy parts E_i^{Img} and E_i^{Real}, is a way to avoid the case of the deformable model being trapped by the spurious prostate boundaries. As shown in the first row of Fig. 13, the positions that are pointed at by the solid arrow and the dashed arrow, respectively, have almost the same energy E_i^{Img}. Without considering E_i^{Real}, it is easy for the model to be trapped by the boundaries in the region of the dashed arrow. However, by using the energy part E_i^{Real}, our model gradually deforms to the region of the solid arrow, which can be observed in the second row of Fig. 13. The last two rows in Fig. 13 show the final segmentation result in the image of $\tilde{F}_{2,0}^{\text{Img}}(x,y)$, the image of $\tilde{F}_{0,0}^{\text{Real}}(x,y)$, and the original TRUS image, respectively.

The third example shows the robustness of our approach with respect to imperfect initialization. It should be mentioned here that the initialization result is not guaranteed to be perfect. Owing to the noisy nature of the ultrasound image and the sparse sampling in initialization parameter space, the initialization could be attracted by local minima. As shown in the upper-left corner of Fig. 14, the automatic initialization, which is denoted by the solid contour, is far from the actual position

TABLE I
COMPARISON OF THE MANUAL SEGMENTATIONS AND THE ALGORITHM-BASED
SEGMENTATIONS

Images in Fig 15	Average Distance (Pixels)	Overlap Area Error (%)	Area Error (%)
Image1	2.6	4.55	5.40
Image2	4.3	4.26	1.25
Image3	2.3	3.43	1.18
Image4	2.6	3.29	2.20
Image5	3.3	5.66	0.77
Image6	3.4	3.20	2.05
Image7	4.6	4.66	0.09
Image8	2.5	2.76	0.34
Mean	**3.20**	**3.98**	**1.66**
Stand. Deviation	0.87	0.97	1.68

of the prostate. The intermediate results in Fig. 14 show that the model gradually moves to reflect the expected position of the prostate with the increase of the iterations. Finally, our algorithm produces a good segmentation result, which is shown in the right-bottom corner of Fig. 14.

Finally, we validated our algorithm by comparing the algorithm-based segmentations and the manual segmentations on the eight US images. Fig. 15 visually shows these results, where the dashed contours are the manual segmentation results and the solid contours are the algorithm-based segmentation results. Moreover, we used the average distances, the overlap area errors and the area errors [19] to show the differences between the algorithm-based segmentations and the manual segmentations. Table I summarizes these values. The average distances range from 2.3 to 4.6 pixels, with the mean at 3.20 pixels. Notably, the pixel sizes in x and y directions are the same, i.e., 0.4 mm. The overlap area errors are from 2.76% to 5.66%, with the mean at 3.98%. The area errors range from 0.09% to 5.40%, with the mean at 1.66%.

The speed of our algorithm has been tested on a 500 MHz processor of SGI workstation. The average running time for segmenting one subject is about 64.0 s, in which about 43.6 s is used for Gabor feature calculation, 0.8 of a second for initialization and 19.6 s for the deformable segmentation.

IV. CONCLUSION

A statistical prostate shape model has been presented in this paper, for the automatic segmentation of prostates in TRUS images. The proposed method has two innovations. First, because of the characteristics of the US image, we employ Gabor filter bank to represent the image features around the prostate boundaries in a multiscale and multiorientation fashion. It is important to use the Gabor features as image features to drive the deformation of the prostate model, because the multioriented Gabor filters provide edge directions as well as edge strengths to correctly distinguish the prostate boundaries. The multiscaled Gabor filters produce coarse as well as fine image features that enable our model to adaptively focus on particular features in the various deformation stages, i.e., coarse features first and fine features later. Second, to make our model robust to local minima, several hierarchical deformation strategies have been presented, including the hierarchical focus of the Gabor features

in different deformation stages, and the hierarchical searching range and curve segment length for each driving point.

The proposed approach has been evaluated on typical TRUS images. The experimental results are promising and show that our approach can outline the prostate boundary from these TRUS images efficiently and accurately, compared to the manual raters. We plan a large scale validation study of our method in the future.

We believe we can continue to improve our methodology in the following aspects. First, we are investigating a more accurate initialization approach. Currently, we rigidly transform the average shape model for making the initialized model optimally matching with the image features in the TRUS image. This is also one of the reasons that the initialization results are not good enough for some images. In the future, we will use several principal eigenvectors of the prostate shape statistics to deform the average shape model, and then rigidly transform the deformed average models to the space of the patient's TRUS image for the optimal initialization. Second, the statistics of the Gabor features around the prostate boundaries can be obtained from a set of training samples, and can be used to statistically define the similarity between the subject and the model.

REFERENCES

[1] (2002) Cancer Facts and Figures 2002. Amer. Cancer Soc.. [Online]http://www.cancer.org
[2] C. Mettlin, "American society national cancer detection project," *Cancer*, vol. 75, pp. 1790–1794, 1995.
[3] K. K. Hodge, J. E. McNeal, M. K. Terris, and T. A. Stamey, "Random-systematic versus directed ultrasound-guided core-biopsies of the prostate," *J. Urol.*, vol. 142, pp. 71–75, 1989.
[4] P. D. Grimm, J. C. Balsko, and H. Ragde, "Ultrasound guided transperineal implantation of iodine 125 and palladium 103 for the treatment of early stage prostate cancer," *Atlas Urol. Clin. North Amer.*, vol. 2, pp. 113–125, 1994.
[5] C. R. Hill and G. R. ter Haar, "High intensity focused ultrasound potential for cancer treatment," *Brit. J. Radiol.*, vol. 68, pp. 1296–1303, 1995.
[6] M. K. Terris and T. A. Stamey, "Determination of prostate volume by transrectal ultrasound," *J. Urol.*, vol. 145, pp. 984–987, 1991.
[7] C. Knoll, M. Alcaniz, V. Grau, C. Monserrat, and M. C. Juan, "Outlining of the prostate using snakes with shape restrictions based on the wavelet transform," *Pattern Recognit.*, vol. 32, pp. 1767–1781, 1999.
[8] A. Ghanei, H. Soltanian-Zadeh, A. Ratkesicz, and F. Yin, "A three-dimensional deformable model for segmentation of human prostate from ultrasound image," *Med. Phys.*, vol. 28, pp. 2147–2153, 2001.
[9] R. Rao and J. Ben-Arie, "Optimal edge detection using expansion matching and restoration," *IEEE Trans. Pattern Anal. Machine Intell.*, vol. 16, pp. 1169–1182, Dec. 1994.
[10] S. D. Pathak, V. Chalana, D. R. Haynor, and Y. Kim, "Edge-guided boundary delineation in prostate ultrasound images," *IEEE Trans. Med. Imag.*, vol. 19, pp. 1211–1219, Dec. 2000.
[11] T. Cootes, A. Hill, C. Taylor, and J. Haslam, "The use of active shape models for locating structures in medical images," *Image Vis. Comput.*, vol. 12, pp. 355–366, 1994.
[12] T. Cootes, D. Cooper, C. Taylor, and J. Graham, "Active shape models—their training and application," *Comput. Vis. Image Understand.*, vol. 61, pp. 38–59, 1995.
[13] N. Duta and M. Sonka, "Segmentation and interpretation of MR brain images: an improved active shape model," *IEEE Trans. Med. Imag.*, vol. 17, pp. 1049–1062, Dec. 1998.

[14] D. Shen, E. H. Herskovits, and C. Davatzikos, "An adaptive-focus statistical shape model for segmentation and shape modeling of 3D brain structures," *IEEE Trans. Med. Imag.*, vol. 20, pp. 257–270, Apr. 2001.

[15] D. Shen and C. Davatzikos, "An adaptive-focus deformable model using statistical and geometric information," *IEEE Trans. Pattern Anal. Machine Intell.*, vol. 22, pp. 906–913, Aug. 2000.

[16] B. S. Manjunath and W. Y. Ma, "Texture features for browsing and retrieval of image data," *IEEE Trans. Pattern Anal. Machine Intell.*, vol. 18, pp. 837–842, Aug. 1996.

[17] D. Shen and C. Davatzikos, "HAMMER: Hierarchical attribute matching mechanism for elastic registration," *IEEE Trans. Med. Imag.*, pp. 1421–1439, Nov. 2002.

[18] A. Fenster and D. Downey, "Three-dimensional ultrasound imaging," *SPIE: Med. Phys.*, vol. 3659, pp. 2–11, 1999.

[19] D. Shen and C. Davatzikos, "Very high resolution morphometry using mass-preserving deformations and HAMMER elastic registration," *NeuroImage*, vol. 18, pp. 28–41, Jan. 2003.

[20] T. F. Cootes, G. J. Edwards, and C. J. Taylor, "Active appearance models," in *Proc. 5th Eur. Conf. Computer Vision*, vol. 2, H. Burkhardt and B. Neumann, Eds., 1998, pp. 484–489.